

Mechanism and improvement strategy of CoSe capacity change during lithiation/delithiation

Qingtao Wang, Minmin Hou, Dongxu Liu, Xiaozhong Zhou, Ziqiang Lei



PII: S0925-8388(20)34462-5

DOI: <https://doi.org/10.1016/j.jallcom.2020.158099>

Reference: JALCOM158099

To appear in: *Journal of Alloys and Compounds*

Received date: 26 September 2020

Revised date: 16 November 2020

Accepted date: 23 November 2020

Please cite this article as: Qingtao Wang, Minmin Hou, Dongxu Liu, Xiaozhong Zhou and Ziqiang Lei, Mechanism and improvement strategy of CoSe capacity change during lithiation/delithiation, *Journal of Alloys and Compounds*, (2020) doi:<https://doi.org/10.1016/j.jallcom.2020.158099>

This is a PDF file of an article that has undergone enhancements after acceptance, such as the addition of a cover page and metadata, and formatting for readability, but it is not yet the definitive version of record. This version will undergo additional copyediting, typesetting and review before it is published in its final form, but we are providing this version to give early visibility of the article. Please note that, during the production process, errors may be discovered which could affect the content, and all legal disclaimers that apply to the journal pertain.

© 2020 Published by Elsevier.

Mechanism and improvement strategy of CoSe capacity change during lithiation/delithiation

Qingtao Wang ^{*a}, Minmin Hou ^a, Dongxu Liu ^a, Xiaozhong Zhou ^a, Ziqiang Lei ^a

a Key Laboratory of Eco-functional Polymer Materials of the Ministry of Education, Key Laboratory of Eco-environmental Polymer Materials of Gansu Province, College of Chemistry and Chemical Engineering, Northwest Normal University, Lanzhou 730070, China

E-mail: wangqt@nwnu.edu.cn

Abstract: Studying the reaction mechanism of materials in the process of lithiation/delithiation is important to understand and optimize the electrode materials. In this work, the petal-like CoSe is prepared by a simple hydrothermal method, and its lithium storage mechanism is studied. During the charge/discharge cycles, the capacity of the CoSe decreases first and then increases. In the initial stage, the volume of CoSe expands due to the intercalation of lithium ions, which results in the amorphousness of CoSe and reduces the specific capacity. The subsequent increase in capacity is due to the recrystallization of the material and the formation of a conductive SEI film. The petal-like CoSe displays a specific capacity of 450 mA h g⁻¹ at the current density of 100 mA g⁻¹ after 300 cycles. To improve the lithium storage performance, a CoSe/rGO composite is prepared. The addition of GO during the preparation of CoSe changes the morphology of CoSe from a larger petal shape to a

smaller rod shape, which weakens the effect of volume change during lithium ion intercalation and shortens the lithium ion diffusion distance, so improves the reduction of specific capacity. At a current density of 100 mA g^{-1} , the specific capacity of CoSe/rGO composite can be as high as 730 mA h g^{-1} after 200 cycles. Even under a large current density of 1000 mA g^{-1} , the specific capacity of the CoSe/rGO composite can still reach 570 mA h g^{-1} after 1000 cycles.

Keywords: CoSe/rGO; lithium storage mechanism; crystal structure; lithium ion batteries

1. Introduction

With the development of society, the secondary lithium-ion batteries have become the main source of power for portable electronic products [1]. Compared with other energy storage materials, lithium-ion batteries have attracted much attention due to their large energy density [2-3]. At present, commercial graphite electrodes have lower theoretical specific capacity (372 mA h g^{-1}). So, looking for alternative high-capacity materials is extremely urgent [4-6].

Transition metal chalcogenides (TMCs) have become an alternative anode material for lithium-ion batteries due to their large theoretical capacity [7-9]. Compared with sulfides, metal selenides have higher conductivity and larger interlayer spacing. Thereby, the charge transfer resistance and electron transfer resistance can be reduced [10-12], which makes them have better lithium storage properties. Besides, because it undergoes a conversion reaction during the lithium ion intercalation process, the

formed Se can increase the specific capacity [13-15]. Therefore, it is expected to become a more promising anode material for lithium ion batteries. However, due to the large volume expansion of the selenide during the charge and discharge process, the material is easily pulverized, which reduces its lithium storage capacity [16-17]. Faced with these shortcomings of metal selenide, the researchers mainly reduce the influence of volume changes through nanometerization and composite with carbon materials. For example, MoSe₂/CNT [18], Co_{0.85}Se/GO [19], SnSe/carbon [20], and MoSe₂@CoSe/NC [21] et al.

The fabrication of the electrode is also an important issue [22-23]. In this work, the petal-like Co(OH)₂ was prepared by a simple hydrothermal method. The CoSe material was further obtained by hydrothermal selenization, which retains its precursor's morphology. The obtained CoSe was used as an electrode material for lithium ion batteries. The cycle performance of CoSe showed a "U" shaped curve, which was first reduced and then increased. Through an in-depth study of CoSe materials with different charge/discharge cycles, the mechanism of charge and discharge reaction of CoSe was revealed. On this basis, the CoSe/rGO composite was prepared by adding GO during the preparation of CoSe. The specific capacity was up to 730 mA h g⁻¹ after 200 cycles at the current density of 100 mA g⁻¹. Even under a large current density of 1000 mA g⁻¹, the specific capacity of the CoSe/rGO composite can still reach 570 mA h g⁻¹ after 1000 cycles.

2. Experimental section

2.1. Material preparation

2.1.1. Materials

All chemical reagents in our experiments are of analytical grade, including cobalt nitrate ($\text{Co}(\text{NO}_3)_2$, Maclean), sodium borohydride (NaBH_4 , Sinopharm Group), and selenium powder (Se, Maclean).

2.1.2. Preparation of $\text{Co}(\text{OH})_2$:

Typically, 5 mmol of $\text{Co}(\text{NO}_3)_2 \cdot 6\text{H}_2\text{O}$ and 10 mmol of hexamethylenetetramine (HMT) were dissolved in 35 mL of deionized water. The solution was transferred to a 50 mL of Teflon-lined stainless-steel autoclave and heated for 12 h at 100 °C. After natural cooling to room temperature, the green product was centrifuged and washed thoroughly with ethanol several times. Subsequently, the product was dried at room temperature for 24 h.

2.1.3. Preparation of CoSe :

2.64 mmol of NaBH_4 and 1 mmol of Se powder were dissolved in 15 mL of deionized water via vigorous stirring for 10 min to obtain a NaHSe solution. Then, 1 mmol of prepared $\text{Co}(\text{OH})_2$ were added to this solution. The resultant suspension was transferred into a 50 mL of Teflon-lined stainless-steel autoclave. After heating for 10 h at 140 °C, the autoclave was cooled to room temperature, and the solid was

centrifuged and washed thoroughly with ethanol several times. Finally, the product was dried at 60 °C overnight in vacuum.

2.1.4. Preparation of CoSe/rGO:

The graphene oxide (GO) was prepared via a modified Hummers' method in our previous work[24]. The Co(OH)₂/rGO composites were prepared via the same reaction conditions mentioned above with the addition of 35 mL 8.68 g L⁻¹ GO aqueous solution. Then, Co(OH)₂/rGO was converted into CoSe/rGO by the same method as described above.

2.2. Materials Physical characterizations

The morphology and elemental mapping of the samples were observed by field emission scanning electron microscope (FESEM, Germany, Carl Zeiss Ultra Plus), transmission electron microscopy (TEM, United States, FEI TECNAI TF20), and energy dispersive spectrometer (EDS, UK, X-Max 80). The structures of the samples were measured on the power X-ray diffractometer (XRD, Germany, Bruker D8 advance) with Cu K_α radiation ($\lambda = 0.15416$ nm). The surface elements of the samples were analyzed with X-ray photoelectron spectroscopy (XPS, US, PHI-5702). The degree of redox and defects of GO were analyzed by Raman spectroscopy (Raman, Germany, RFS 100/S). The content of the CoSe/rGO composites was determined by thermogravimetric analysis (TGA, Germany, Netzsch STA449F3). The Brunauer-Emmett-Teller (BET) specific surface areas were obtained by evaluating N₂

adsorption-desorption isotherms obtained on an Autosorb-iQ2-MP adsorption instrument.

2.3. Electrochemical measurements

The prepared sample, conductive carbon black, and polyvinylidene fluoride (PVDF) binder were ground in a mortar at a mass ratio of 8:1:1. The mixture was then dispersed in N-methyl-2-pyrrolidone (NMP) and stirred 6-8 h to form a uniform slurry. The obtained slurry was coated on Cu foil with a typical mass loading of ~ 1 mg cm⁻² and dried in a vacuum oven at 60 °C for 12 h. Li foil was used as the counter electrode and Celgard 2400 polypropylene film as the separator. 1.0 M LiPF₆ solution (EC:DEC = 1:1 vol.%) and 5.0 wt.% of fluoroethylene carbonate (FEC) were chosen as electrolyte. The electrode materials were assembled into a 2025-type half-cell in an argon-filled glove box.

The cycle performance carried out on a battery testing system (LANHE CT2001A, Wuhan LAND electronic Co. Ltd., China) with a voltage range of 0.01-3.0 V (vs. Li⁺/Li). The cyclic voltammetry (CV) and electrochemical impedance spectroscopy (EIS) tests were performed on an Autolab PGSTAT128N electrochemical workstation (Metrohm, Switzerland). The CV test was tested at a scan rate of 0.1 mV s⁻¹ within 0.01-3.0 V (vs. Li⁺/Li). The EIS measurements were measured with an alternating voltage of 10 mV over the frequency range from 10⁵ to 10⁻² Hz. After cycling, the batteries were disassembled in an argon-filled glove box. The obtained electrodes

were rinsed with dimethyl carbonate and dried in the glove box overnight for TEM, XRD, and XPS testing.

3. Results and discussion

The X-ray diffraction (XRD) patterns of the CoSe and CoSe/rGO are presented in the supplementary material (Fig. S1). It can be easily seen that the prepared CoSe and CoSe/rGO are consistent with hexagonal CoSe (ICDD PDF#70-2870). The diffraction peaks at 33.2° , 44.8° , and 50.4° correspond to the (101), (102), and (110) crystal planes of CoSe, respectively. The broadening of the diffraction peak of CoSe is obvious, indicating that the size of the prepared CoSe is small. The intensity of the diffraction peak of CoSe/rGO is lower, which indicates that the crystallinity is lower or the grain size is smaller.

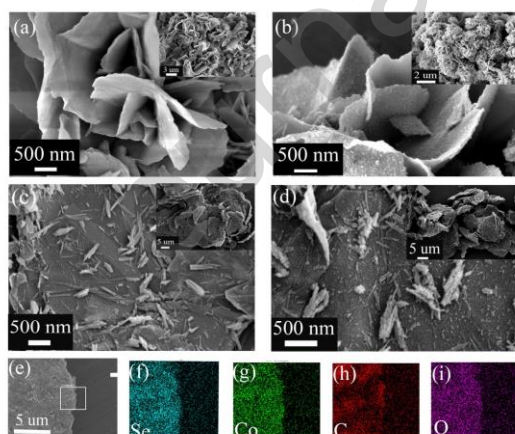


Fig. 1. SEM images of (a) Co(OH)_2 , (b) CoSe, (c) $\text{Co(OH)}_2/\text{rGO}$ composite, (d) CoSe/rGO composite. The insets correspond to the low magnification SEM images of each samples. EDS elemental mappings of (e-i) CoSe/rGO, Se, Co, C, and O.

As shown in Fig. 1a and the inset, the precursor Co(OH)_2 is a petal-like structure with a smooth surface. Fig. 1b and inset show that the as-prepared CoSe also maintains the petal-like morphology, but the surface changed rougher. The SEM image of the precursor $\text{Co(OH)}_2/\text{rGO}$ is shown in Fig. 1c. The nano-scale rod-like Co(OH)_2 is distributed on the surface of the rGO sheet. It can be seen from Fig. 1d that the structure of CoSe/rGO was substantially unchanged after selenization, and some rod-like Co(OH)_2 of the surface were pulverized into nanoparticles. The EDS elemental mappings of CoSe/rGO in Fig. 1e-i show that Se, Co, C, and O are uniformly distributed. The presence of O may be due to partial oxidation of the surface of CoSe/rGO.

Transmission electron microscopy (TEM) images of the as-prepared CoSe are shown in Fig. S2a. It can be seen that the CoSe material is a sheet-like morphology. Fig. S2b shows an HRTEM image of CoSe, in which the clear lattice spacing of 0.149, 0.313, and 0.122 nm correspond to the (112), (100), and (104) plane of CoSe. Fig. S2c corresponds to the TEM image of CoSe/rGO. It can be seen that the CoSe nanorods grown on the rGO sheets. In Fig. S2d, the lattice fringes of 0.181 nm, 0.156 nm, and 0.264 nm correspond to the (110), (200), and (002) crystal planes of CoSe, respectively. The lattice fringes of 0.34 nm correspond to the interlayer distance of rGO. This result indicates that the CoSe/rGO composite was successfully prepared.

The pore size distribution and specific surface area of the material can be quantitatively analyzed by evaluating nitrogen adsorption-desorption isotherms (Fig.

S3). The Brunauer–Emmett–Teller (BET) specific surface areas of the CoSe and CoSe/rGO was $33.51 \text{ m}^2 \text{ g}^{-1}$ and $40.21 \text{ m}^2 \text{ g}^{-1}$, respectively. CoSe/rGO has a larger specific surface area, which facilitates the exposure of more catalytic sites. It can be seen from the pore size distribution map that the mesopores of the material are mainly distributed below 15 nm.

The CoSe/rGO composites were tested for carbon content by TG analysis, as shown in Fig. S4a. The slight weight lost below $150 \text{ }^\circ\text{C}$ is the evaporation of water. The mass lost between 200 and $600 \text{ }^\circ\text{C}$ is the oxidation of rGO and CoSe material. Based on the chemical reaction of $3\text{CoSe (s)} + 5\text{O}_2 \text{ (g)} = \text{Co}_3\text{O}_4 \text{ (s)} + 3\text{SeO}_2 \text{ (g)}$ [25-28], the contents of the CoSe and rGO were calculated to be 58.3 wt.% and 41.7 wt.%, respectively. The Raman spectrum also confirmed the existence of rGO in the CoSe/rGO composite. As presented in Fig. S4b, there are two peaks at the 1344 cm^{-1} and the 1596 cm^{-1} , corresponding to the D-band and G-band of rGO. I_D/I_G ratio value is 1.05, implying a higher degree of defects, which is favorable to ion intercalation/deintercalation and improve the electrochemical properties [29].

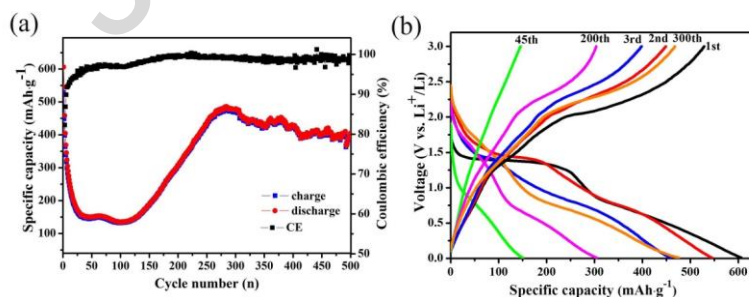


Fig. 2. (a) the cyclic performance of CoSe at the current density of 100 mA g^{-1} and (b) corresponding discharge/charge curves.

The electrochemical performance of CoSe is shown in Fig. 2. Fig. 2a is the cycle performance of CoSe at the current density of 0.1 A g^{-1} . It can be seen that the initial discharging specific capacity is $606.4 \text{ mA h g}^{-1}$ and coulomb efficiency is 82.2%. Before the 30th cycle, the specific capacity is gradually reduced. Between the 30th and 120th cycles, the specific capacity is maintained at about 150 mA h g^{-1} . After 120th cycles, the specific capacity gradually rose. After 500th cycles, it was about 400 mA h g^{-1} . The galvanostatic charge/discharge curves are shown in Fig. 2b. It can be seen that the reaction platforms for intercalation/deintercalation of lithium ion are clear in the initial three cycles. However, the curve of the 45th cycle shows almost no obvious platform. Interestingly, in the curves of the 200th and 300th cycles, similar reaction platforms can be seen clearly. The CoSe exhibits strange cycle performance and charge/discharge curves. To understand the intercalation/de-intercalation mechanism of lithium ion, we selected samples of the 45th and 200th cycles for further analysis.

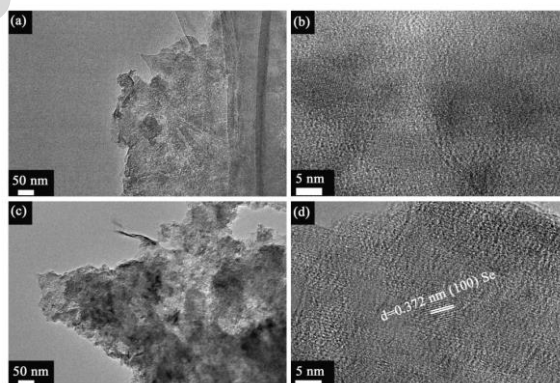


Fig. 3. TEM and HRTEM images of CoSe after (a), (b) 45th cycles and (c), (d) 200th cycles.

The TEM image of CoSe after the 45th cycles in the full lithiation state is shown in Fig. 3a. It can be seen that the CoSe material is a sheet-like morphology. Fig. 3b displays a high-resolution TEM image of CoSe after the 45th cycles, and there are no clear crystal regions. Fig. 3c and d show the structure of CoSe after the 200th cycles in the full lithiation state. In Fig. 3c, it can be found that small nanoparticles distributed on the sheet-like materials. Fig. 3d exhibit the lattice fringe of 0.372 nm, corresponding to the (100) plane of Se, which matches with the XRD results (Fig. 4b). The magnified images of Fig. 3b and d are shown in Fig. S5.

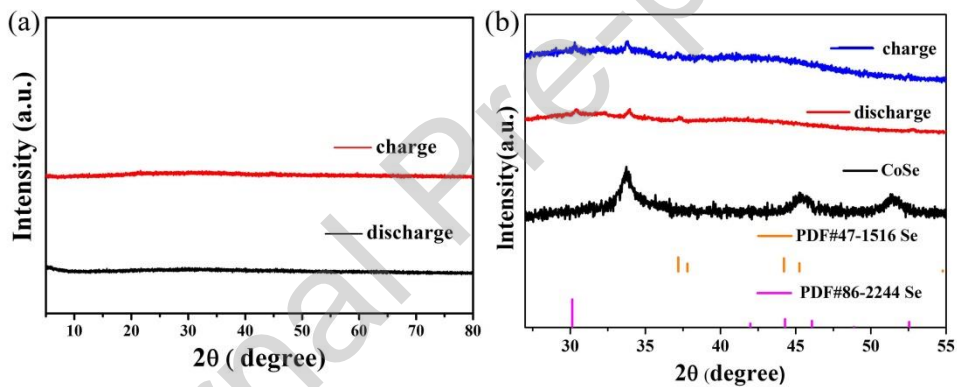


Fig. 4. XRD patterns of CoSe after (a) 45th and (b) 200th cycles.

Fig. 4a shows the XRD patterns of the CoSe material fully discharged and fully charged after 45th cycles. It can be seen that the CoSe, whether fully charged or discharged, has no diffraction peaks and is amorphous. Fig. 4b is the XRD patterns of CoSe material after 200th cycles, whether fully charged or discharged, the spectra have the same diffraction peaks, corresponding to CoSe and two different structures of Se. When fully discharged, the CoSe and Se were not completely involved in the intercalation reaction of lithium ion. Moreover, the diffraction peaks of Li_2Se and Co

were not detected after the 45th and 120th cycles, indicating that the product formed is amorphous during the intercalation of lithium ion.

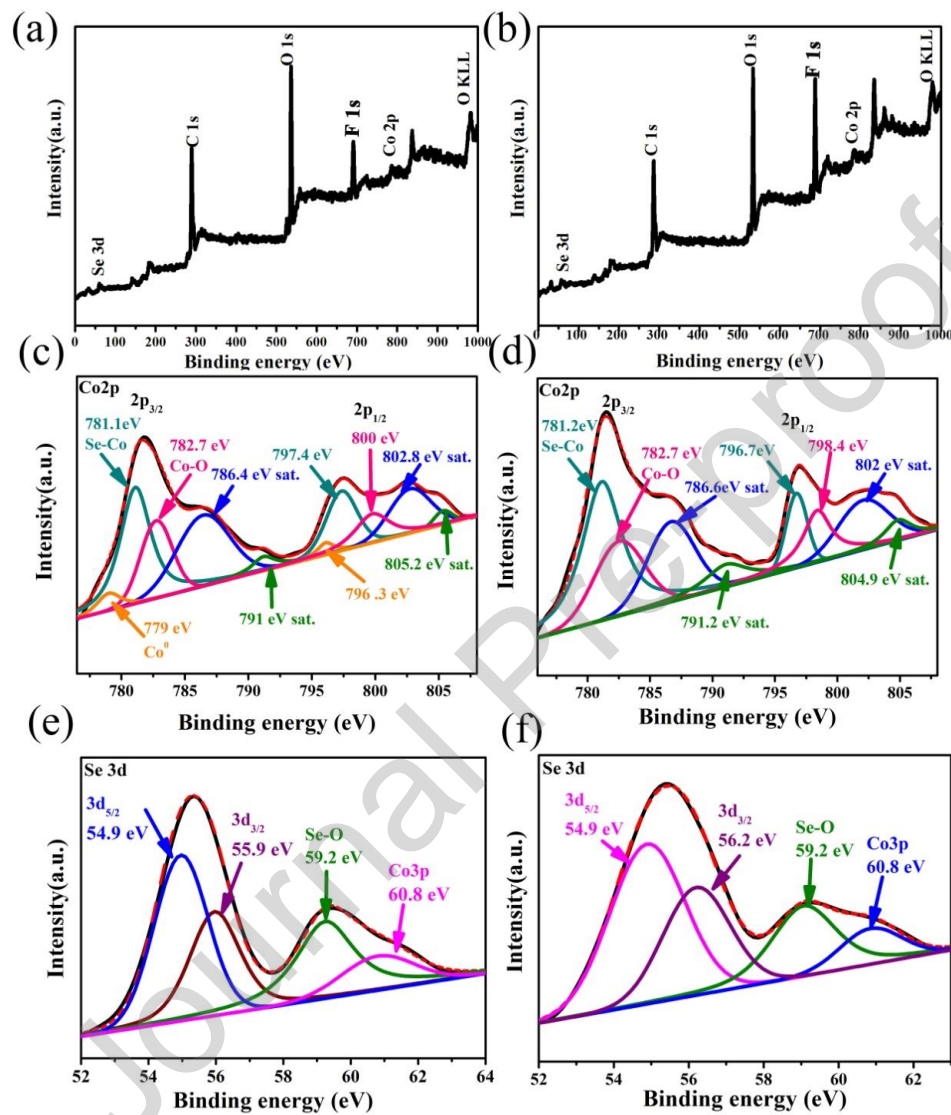


Fig. 5. XPS spectra of the CoSe samples after 45th cycles. (a) XPS survey spectrum of fully discharged state, (b) XPS survey spectrum of fully charged state, (c) high-resolution Co 2p XPS spectrum of fully discharged state, (d) high-resolution Co 2p XPS spectrum of fully charged, (e) high-resolution Se 3d XPS spectrum of fully discharged state, and (f) high-resolution Se 3d XPS spectrum of fully charged.

Fig. 5a and b show the XPS survey spectra of the CoSe material in the fully discharged and fully charged state after 45th cycles, respectively. It can be seen that the CoSe material surface contains Se, Co, and O elements in the fully discharged and fully charged state, where O may be derived from adsorption of oxygen or oxidation of the surface of the material. The sharp and strong peaks at about 690 eV can be ascribed to the F element due to the residual electrolyte in the electrode. The high-resolution Co 2p XPS spectrum of the CoSe samples in the fully discharged state after 45th cycles is shown in Fig. 5c. The two peaks located at 779.0 and 796.3 eV can be assigned to $\text{Co}^0 2p_{3/2}$ and $\text{Co}^0 2p_{1/2}$, respectively. It can be seen that the content of metallic Co is very small. Two peaks appeared at 781.1 and 797.4 eV, corresponding to $\text{Co}^{2+} 2p_{3/2}$ and $\text{Co}^{2+} 2p_{1/2}$ of CoSe, respectively. In addition, the peaks at 782.7 and 800 eV can be ascribed to $\text{Co}^{2+} 2p_{3/2}$ and $\text{Co}^{2+} 2p_{1/2}$ of CoO [10,30,31]. Meanwhile, the other peaks are satellite peaks [32]. Fig. 5d shows the high-resolution Co 2p spectrum of the CoSe samples in the fully charged state after 45th cycles. The binding energies of Co $2p_{3/2}$ and Co $2p_{1/2}$ of CoSe were identified at 781.2 and 796.7 eV, respectively. The two peaks at 782.7 and 798.4 eV can be ascribed to $\text{Co}^{2+} 2p_{3/2}$ and $\text{Co}^{2+} 2p_{1/2}$ of CoO. The other peaks are satellite peaks. Compared to the fully discharged state, there are no binding energies of $\text{Co}^0 2p_{3/2}$ and $\text{Co}^0 2p_{1/2}$. Fig. 5e and f show high-resolution XPS spectra of Se 3d in the fully discharged state and fully charged state after 45th cycles. It can be seen that except for the peaks of $3d_{5/2}$ and $3d_{3/2}$ of Se^{2-} [31,33], the binding energy located at 59.2 eV can be ascribed to the

partial surface oxidation of Se. The peaks that appeared at 60.8 eV can be assigned to the binding energy of Co 3p [20, 32].

Fig. S6a and b show the XPS survey spectra of the CoSe material in the fully discharged and fully charged state after 200th cycles, respectively. It can be seen that after 200th cycles, only Se was detected on the surface of the material, and Co was not detected. Similarly, Co was hardly detected in the high-resolution Co 2p spectra in Fig. S6c and d. Interestingly, Se can be detected in the high-resolution Se 3d XPS spectra in Fig. S6e and f. This phenomenon may be due to after 200th cycles, the formed Se dissolved and became a component of the solid electrolyte interface (SEI) film [34-35]. As the number of charge/discharge cycles increases, a thicker SEI film was formed. XPS can only detect elements on the surface of the material. So after 200th cycles, only Se was detected, and Co was not detected.

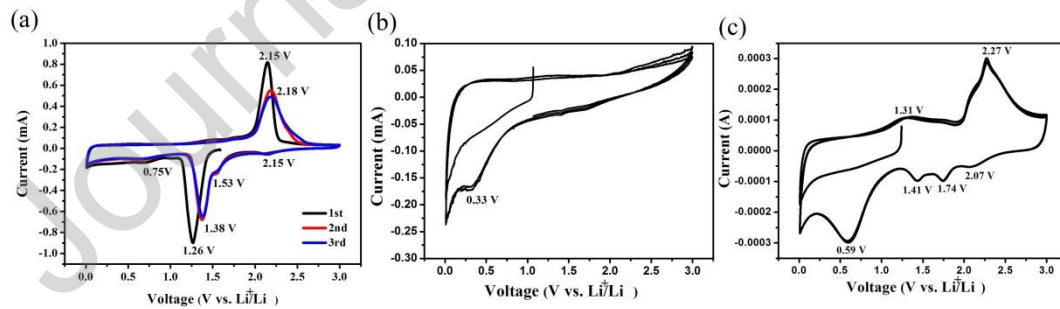


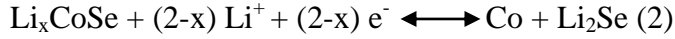
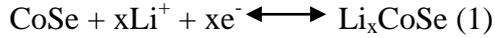
Fig. 6. CV curves of CoSe at the scan rate of 0.1 mV s^{-1} . (a) initial three cycles, (b) after 45th cycles, and (c) after 200th cycles.

Fig. 6 is the CV curves of CoSe at different charge/discharge cycles. According to reports, the lithium storage mechanism of CoSe is a multi-step reaction process [36-37]. Fig. 6a shows the CV curves of the first three cycles of the CoSe at the scan

rate of 0.1 mV s^{-1} and voltage range from 0.01 to 3 V vs. Li^+/Li . During the first cathodic scan, the peak at 2.15 V can be ascribed to the lithium insertion, and the peak at 1.26 V corresponds to the sequential lithium insertion of CoSe to Li_xCoSe and the formation of SEI film, and the peak at 0.75 V can be attributed to the formation of metallic Co and Li_2Se [36,38,13,28]. In the anodic scan, the peak at 2.15 V corresponds to the delithiation process [34,37]. In the subsequent 2nd and 3rd cycle's curves, the two cathodic peaks at 1.53 and 1.38 V correspond to the formation of Li_xCoSe . Meanwhile, the cathodic peak at 0.75 V also ascribes to the formation of Li_2Se and Co [39]. The anodic peaks from 2.15 V to 2.18 V could be attributed to the delithiation processes, similar to the previously reported results [28,37]. Compared with the CV curves of the first three cycles, the CV curves after 45th cycles in Fig. 6b can be observed only one cathodic peak, which moved to 0.33 V, indicating that lithium intercalation behavior became more difficult. In combination with the XRD analysis in Fig. 4a, it was found that CoSe formed an amorphous structure during the 45th charge/discharge cycles.

Fig. 6c is the CV curves of CoSe after 200th cycles, significantly different from the CV curves of the first three cycles and after the 45th cycles. According to the XRD analysis of Fig. 4b, the electrode material not only contained CoSe, but also generated Se after 200th cycles. The cathodic peak of 2.07 V corresponds to the insertion of Li^+ into Se, and the two cathodic peaks at 1.74 V and 1.41 V correspond to the insertion of Li^+ into CoSe to form Li_xCoSe [36-37]. The cathodic peak at 0.59 V can be attributed to the insertion of Li^+ into Li_xCoSe , which is converted into Co and Li_2Se [28,36]. In the anodic scan, the peak at 1.31 V and 2.27 V are attributed to the gradual delithiation processes and reversibly forming CoSe and Se [36-37,39-40].

Based on the above analysis and relevant literature, the reaction mechanism of the CoSe during the entire charge/discharge cycles can be described as follows:



As shown in Fig. 2a, the cycle performance of CoSe shows a “U” shaped curve. During the first 45th cycles, the structure of the material gradually changed and produced an amorphous material. The cathodic peak in the CV curve shifted to a lower potential, indicating that lithium intercalation behavior became more difficult, resulting in capacity degradation. However, after 200th cycles, the material gradually changed from amorphous to crystalline structure and the capacity gradually increased. On the other hand, Se is partially dissolved and became a component of the SEI film. The formed conductive SEI film can facilitate charge transfer [34-35]. Also, the reversible growth of the SEI film during charge and discharge can increase the capacity [41-42].

Fig. S7 shows the Nyquist plots of CoSe electrodes after 45th and 200th charge/discharge cycles. It can be found that after the 45th cycles, the diameter of the semicircle in the high frequency range is larger than that of after the 200th cycles. The result indicates that after 200th cycles, the electrode material has better electron conductivity and lower charge transfer resistance. It further illustrates that nanocrystals and conductive SEI films' formation make lithium's insertion/extraction easier.

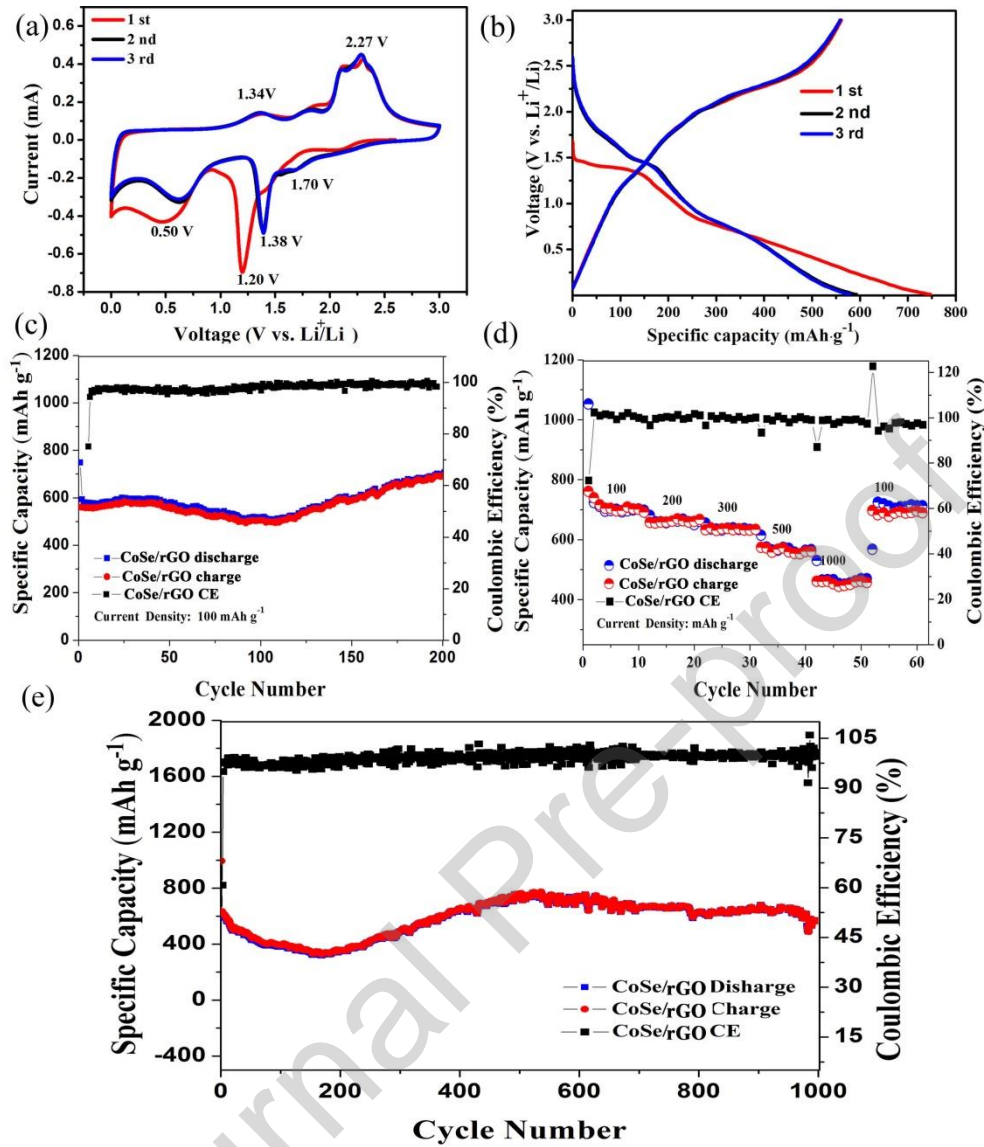


Fig. 7. (a) CV curves of CoSe/rGO at the scan rate of 0.2 mV s⁻¹, (b) initial three discharge/charge curves of CoSe/rGO at the current density of 100 mA g⁻¹, (c) the cycle performance of CoSe/rGO at the current density of 100 mA g⁻¹, (d) rate-performance of CoSe/rGO at the current densities ranging from 100 mA g⁻¹ to 1000 mA g⁻¹, and (e) long-term cycle performance of CoSe/rGO at the current density of 1000 mA g⁻¹.

In Fig. 7a, it is easy to find that the CV curves of CoSe/rGO are similar to that of the pure CoSe material. Fig. 7b is the charge/discharge curves of the first three cycles of CoSe/rGO. It can be seen that due to the formation of the SEI film in the first charge/discharge process, the coulombic efficiency is low. The second and third charge/discharge curves are basically coincident, and the coulombic efficiency is higher. Compared with pure CoSe, the addition of rGO can effectively improve the material's coulombic efficiency and capacity. Fig. 7c shows the cycle performance of the CoSe/rGO composite at a current density of 100 mA g^{-1} . For the first cycle, the coulombic efficiency was 75%. After that, the coulombic efficiency increased rapidly. After the 200th cycles, the specific capacity of CoSe/rGO was as high as 730 mA h g^{-1} , showing good cycling performance. Compared with CoSe, CoSe/rGO has a higher specific capacity, and the specific capacity of CoSe/rGO decreases and increases to a lesser extent during the cycles. It is maybe because the addition of rGO caused CoSe to change from large flakes to small rods, which weakens the effect of volume change during lithium ion intercalation and shortens the lithium ion diffusion distance, so improves the reduction of specific capacity. Besides, the good conductivity of rGO can also promote the cycling performance of the material.

The rate performance of CoSe/rGO at current densities from 100 mA g^{-1} to 1000 mA g^{-1} is shown in Fig. 7d. When the current density gradually increased ($100, 200, 300, 500, \text{ and } 1000 \text{ mA g}^{-1}$), the delivered charge specific capacities were $703, 658, 631, 553, \text{ and } 459 \text{ mA h g}^{-1}$, respectively. More importantly, the specific capacity reached 695 mA h g^{-1} when the current density was reduced back to 100 mA g^{-1} . This

result demonstrates that CoSe/rGO composite has good rate performance. The long-term cycling performance of CoSe/rGO was tested at a current density of 1000 mA g⁻¹ (Fig. 7e). After 1000 cycles, the specific capacity was up to 570 mA h g⁻¹. It indicates that the CoSe/rGO composite has good cycle stability under large current density.

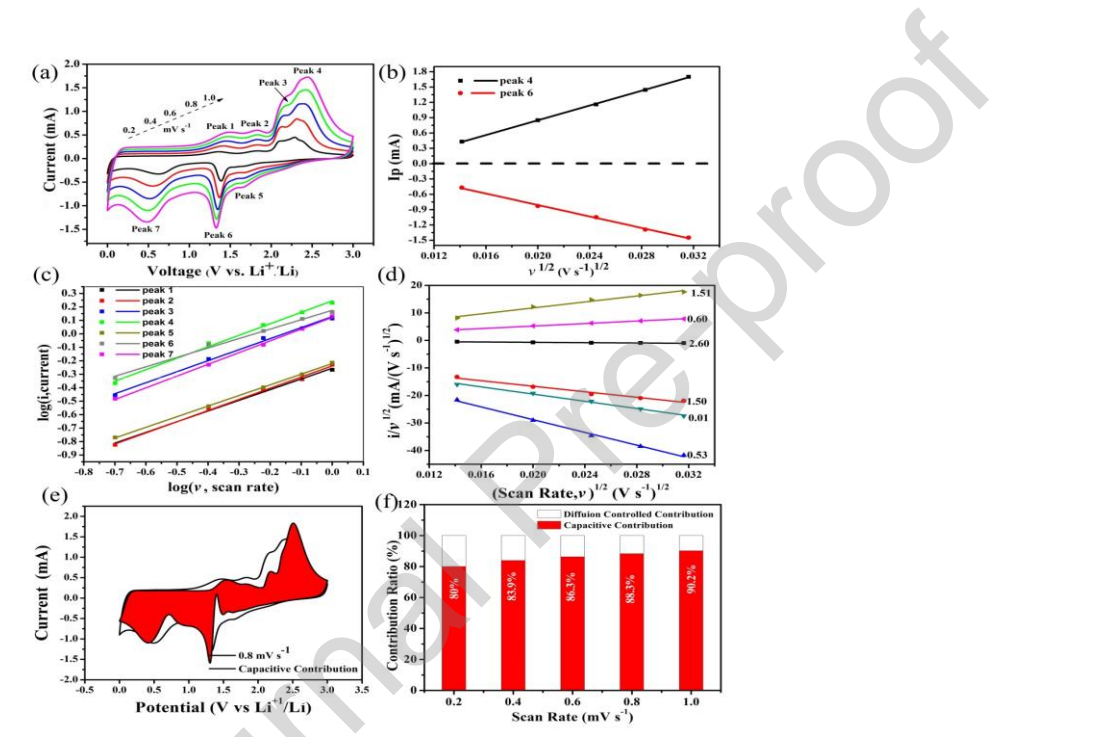


Fig. 8. (a) CV curves of CoSe/rGO at different scan rates from 0.2 to 1.0 mV s⁻¹, (b) the linear relation of peak currents and the square root of scan rate, (c) the linear relation of log (*i*, peak current) and log (*v*, scan rate), (d) plots of $v^{1/2}$ vs. $i/v^{1/2}$ at different redox states for obtaining constants of k_1 and k_2 , (e) capacitive contribution (red) and diffusion controlled contribution (white) at the scan rate of 0.8 mV s⁻¹, (f) contribution ratios of capacitive (red) and diffusion controlled (white) contribution at different sweep rates.

To further study this excellent electrochemical performance of the CoSe/rGO composite, a series of CV tests were carried out at various scan rates. Fig. 8a shows the typical CV curves for CoSe/rGO electrode at the scan rates from 0.2 to 1.0 mV s⁻¹. It can be seen that CoSe/rGO composite has a slight polarization with the increase of scan rates. Fig. 8b shows the relation of the peak currents (I_p , mA) of CV curves and the scan rates' square root ($v^{1/2}$, mV^{1/2} s^{-1/2}). According to previous reports, the relationship between the peak currents and scan rates is as follows [43-45]:

$$i = av^b \quad (4)$$

$$\log i = b \log v + \log a \quad (5)$$

Where a and b are both variable parameters. The value of b determined by the slope of $\log i$ vs. $\log v$ in Eq. (5). If the value of b is near 0.5, the diffusion-controlled behavior, that is, cation intercalation, is prevailing during the charge/discharge process.

Whereas the value of b close to 1 indicates that the capacitive behavior is dominant [46-47]. In this work, the relationship between $\log i$ and $\log v$ is presented in Fig. 8c. It is found that the b values of the four anodic peaks (Peaks 1, 2, 3, and 4) and the cathodic peaks (Peaks 5, 6, and 7) are 0.79, 0.83, 0.82, 0.85, 0.79, 0.70, and 0.87, respectively. It implies that the redox kinetic process of CoSe/rGO composite contains diffusion-controlled and capacitive behaviors.

In addition, the respective contribution of the capacitive and the diffusion-controlled behaviors at a specific scan rate can be quantitatively distinguished at a specific voltage by Eq. (6):

$$i(V) = k_1v + k_2v^{1/2} \quad (6)$$

Here k_1 can be obtained by the slope of $i(V)/v^{1/2}$ vs. $v^{1/2}$ plots. In Eq. (6), k_1v and $k_2v^{1/2}$ represent the capacitive contribution and diffusion-controlled contribution. Based on the above discussion, as shown in Fig. 8d, the fitted line slope is k_1 , and the intercept is k_2 . Fig. 8e displays the capacitive contribution (red) and diffusion controlled contribution (white) at the scan rate of 0.8 mV s^{-1} . The diffusion-controlled contribution is mainly generated at around the redox peak in both lithiation and delithiation processes. Likewise, the contribution ratios of the capacitive and diffusion controlled behaviors at different scan rates were also quantified (Fig. 8f). The results show that the capacitive contribution increases with the increase of the scan rates.

4. Conclusions

In this work, the CoSe and CoSe/rGO composite were prepared by a simple hydrothermal method, and CoSe/rGO exhibited excellent electrochemical performance. In particular, by studying the lithium storage mechanism of the CoSe material, it is found that the material underwent phase transformation during the charge and discharge cycles. After the 45th charge/discharge cycles, CoSe formed an amorphous material. The cathodic peak in the CV curve shifted to a lower potential, indicating that lithium intercalation behavior becomes more difficult, so the specific capacity is reduced. In the subsequent electrochemical cycles, the amorphous materials evolved into CoSe and Se nanocrystals, which increases the specific capacity. Besides, Se is partially dissolved and became a component of the SEI film.

The conductive SEI film can promote the charge transfer, and the reversible growth of SEI film during charge and discharge can increase the capacity. To increase the stability of lithium storage, we prepared CoSe/rGO composite. The addition of rGO caused CoSe to change from larger nanosheets to smaller nanorods, which weakens the effect of volume change during lithium ion intercalation and shortens the lithium ion diffusion distance, so improves the reduction of specific capacity. The good electrical conductivity of rGO also promoted the lithium storage performance of CoSe/rGO composite. After 200th cycles at the current density of 100 mA g^{-1} , the CoSe/rGO composite's specific capacity is 730 mA h g^{-1} . Even under a large current density of 1000 mA g^{-1} , after 1000 cycles, the specific capacity of the CoSe/rGO composite can still reach 570 mA h g^{-1} .

Declaration of Competing interest

The authors declare no competing interests.

Acknowledgments

This work was supported by the National Natural Science Foundation of China (21865032), the Innovation Team Basic Scientific Research Project of Gansu Province (1606RJIA324), the Science and Technology program of Gansu Province (19JR2RA020).

References

- [1] Ko Y N, Choi S H, Kang Y C. Hollow cobalt selenide microspheres: synthesis and application as anode materials for Na-ion batteries. *ACS Applied Materials & Interfaces*, 2016, 8(10): 6449-6456.
- [2] Liu H, Li W, Shen D, et al. Graphitic carbon conformal coating of mesoporous TiO₂ hollow spheres for high-performance lithium ion battery anodes. *Journal of the American Chemical Society*, 2015, 137(40): 13161-13166.
- [3] Reddy M V, Subba Rao G V, Chowdari B V R. Metal oxides and oxysalts as anode materials for Li ion batteries. *Chemical Reviews*, 2013, 113(7): 5364-5457.
- [4] Cui Y H, Xue M Z, Fu Z W, et al. Nanocrystalline CoP thin film as a new anode material for lithium ion battery. *Journal of Alloys and Compounds*, 2013, 555: 283-290.
- [5] Wang Z, Zhou L, Lou X W. Metal oxide hollow nanostructures for lithium - ion batteries. *Advanced Materials*, 2012, 24(14): 1903-1911.
- [6] Guo J, Yang Z, Archer L A. Aerosol assisted synthesis of hierarchical tin-carbon composites and their application as lithium battery anode materials. *Journal of Materials Chemistry A*, 2013, 1(31): 8710-8715.
- [7] Hu H, Zhang J, Guan B, et al. Unusual formation of CoSe@carbon nanoboxes, which have an inhomogeneous shell, for efficient lithium storage. *Angewandte Chemie International Edition*, 2016, 55(33): 9514-9518.

- [8] Wu R, Wang D P, Rui X, et al. In - situ formation of hollow hybrids composed of cobalt sulfides embedded within porous carbon polyhedra/carbon nanotubes for high - performance lithium - ion batteries. *Advanced Materials*, 2015, 27(19): 3038-3044.
- [9] Yu X Y, Hu H, Wang Y, et al. Ultrathin MoS₂ nanosheets supported on N - doped carbon nanoboxes with enhanced lithium storage and electrocatalytic properties. *Angewandte Chemie International Edition*, 2015, 54(25): 7395-7398.
- [10] Huang Y, Wang Z, Jiang Y, et al. Hierarchical porous Co_{0.85}Se@ reduced graphene oxide ultrathin nanosheets with vacancy-enhanced kinetics as superior anodes for sodium-ion batteries. *Nano Energy*, 2018, 53: 524-535.
- [11] Ge P, Hou H, Banks C E, et al. Binding MoSe with carbon constrained in carbonous nanosphere towards high-capacity and ultrafast Li/Na-ion storage. *Energy Storage Materials*, 2018, 12: 310-323.
- [12] Eftekhari A. Molybdenum diselenide (MoSe₂) for energy storage, catalysis, and optoelectronics. *Applied Materials Today*, 2017, 8: 1-17.
- [13] Zhou J, Wang Y, Zhang J, et al. Two dimensional layered Co_{0.85}Se nanosheets as a high-capacity anode for lithium-ion batteries. *Nanoscale*, 2016, 8(32): 14992-15000.
- [14] Li X, Liang J, Li X, et al. High-performance all-solid-state Li-Se batteries induced by sulfide electrolytes. *Energy & Environmental Science*, 2018, 11(10): 2828-2832.

- [15] Li X, Liang J, Luo J, et al. High-Performance Li-SeS_x All-Solid-State Lithium Batteries. *Advanced Materials*, 2019, 31(17): 1808100.
- [16] Hu Z, Liu Q, Chou S L, et al. Advances and challenges in metal sulfides/selenides for next - generation rechargeable sodium - ion batteries. *Advanced Materials*, 2017, 29(48): 1700606.
- [17] Tang Q, Cui Y, Wu J, et al. Ternary tin selenium sulfide (SnSe_{0.5}S_{0.5}) nano alloy as the high-performance anode for lithium-ion and sodium-ion batteries. *Nano Energy*, 2017, 41: 377-386.
- [18] Niu F, Yang J, Wang N, et al. MoSe₂ - Covered N, P - Doped Carbon Nanosheets as a Long - Life and High - Rate Anode Material for Sodium - Ion Batteries. *Advanced Functional Materials*, 2017, 27(23): 1700522.
- [19] Zhang G, Liu K, Liu S, et al. Flexible Co_{0.85}Se nanosheets/graphene composite film as binder-free anode with high Li-and Na-Ion storage performance. *Journal of Alloys and Compounds*, 2018, 731: 714-722.
- [20] Zhang Z, Zhao X, Li J. SnSe/carbon nanocomposite synthesized by high energy ball milling as an anode material for sodium-ion and lithium-ion batteries. *Electrochimica Acta*, 2015, 176: 1296-1301.
- [21] Chen J, Pan A, Wang Y, et al. Hierarchical mesoporous MoSe₂@CoSe/N-doped carbon nanocomposite for sodium ion batteries and hydrogen evolution reaction applications. *Energy Storage Materials*, 2019, 21: 97-106.

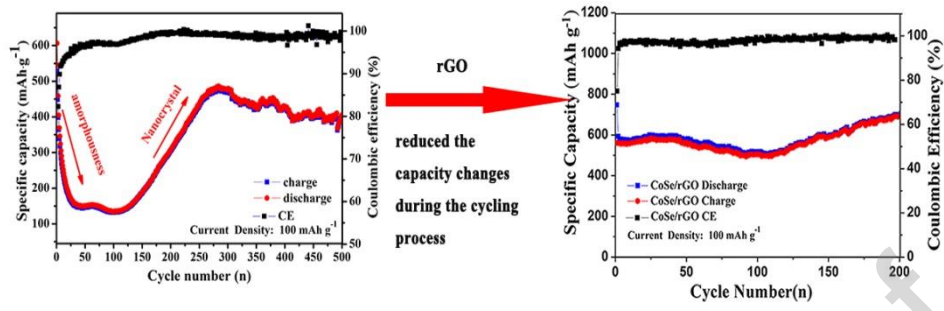
- [22] Tian X, Zhou K. 3D printing of cellular materials for advanced electrochemical energy storage and conversion. *Nanoscale*, 2020, 12: 7416-7432.
- [23] Wei T S, Ahn B Y, Grotto J, et al. 3D Printing of Customized Li-Ion Batteries with Thick Electrodes. *Advanced Materials*, 2018, 30(16): 1703027.
- [24] Zhou X, Zhang Z, Lu X, et al. Sb₂O₃ nanoparticles anchored on graphene sheets via alcohol dissolution–reprecipitation method for excellent lithium-storage properties. *ACS Applied Materials & Interfaces*, 2017, 9(40): 34927-34936.
- [25] Zhang Y, Pan A, Ding L, et al. Nitrogen-doped yolk–shell-structured CoSe/C dodecahedra for high-performance sodium ion batteries. *ACS Applied Materials & Interfaces*, 2017, 9(4): 3624-3633.
- [26] Zhang Z, Shi X, Yang X. Synthesis of core-shell NiSe/C nanospheres as anodes for lithium and sodium storage. *Electrochimica Acta*, 2016, 208: 238-243.
- [27] Hong Y J, Kim J H, Kang Y C. Sodium-ion storage performance of hierarchically structured (Co_{1/3}Fe_{2/3})Se₂ nanofibers with fiber-in-tube nanostructures. *Journal of Materials Chemistry A*, 2016, 4(40): 15471-15477.
- [28] Liu J, Liang J, Wang C, et al. Electrospun CoSe@N-doped carbon nanofibers with highly capacitive Li storage. *Journal of Energy Chemistry*, 2019, 33: 160-166.

- [29] Han K, Liu Z, Li P, et al. High-throughput fabrication of 3D N-doped graphenic framework coupled with Fe₃C@ porous graphite carbon for ultrastable potassium ion storage. *Energy Storage Materials*, 2019, 22: 185-193.
- [30] Zhang H, Yang B, Wu X, et al. Polymorphic CoSe₂ with mixed orthorhombic and cubic phases for highly efficient hydrogen evolution reaction. *ACS Applied Materials & Interfaces*, 2015, 7(3): 1772-1779.
- [31] Li H, Gao D, Cheng X. Simple microwave preparation of high activity Se-rich CoSe₂/C for oxygen reduction reaction. *Electrochimica Acta*, 2014, 138: 232-239.
- [32] Dong Q, Wang Q, Dai Z, et al. MOF-derived Zn-doped CoSe₂ as an efficient and stable free-standing catalyst for oxygen evolution reaction. *ACS Applied Materials & Interfaces*, 2016, 8(40): 26902-26907.
- [33] Kong D, Wang H, Lu Z, et al. CoSe₂ nanoparticles grown on carbon fiber paper: an efficient and stable electrocatalyst for hydrogen evolution reaction. *Journal of the American Chemical Society*, 2014, 136(13): 4897-4900.
- [34] Zhou Y, Tian R, Duan H, et al. CoSe/Co nanoparticles wrapped by in situ grown N-doped graphitic carbon nanosheets as anode material for advanced lithium ion batteries. *Journal of Power Sources*, 2018, 399: 223-230.
- [35] Eom K S, Lee J T, Oschatz M, et al. A stable lithiated silicon–chalcogen battery via synergetic chemical coupling between silicon and selenium. *Nature Communications*, 2017, 8: 13888.

- [36] Li J, Yan D, Lu T, et al. An advanced CoSe embedded within porous carbon polyhedra hybrid for high performance lithium-ion and sodium-ion batteries. *Chemical Engineering Journal*, 2017, 325: 14-24.
- [37] Li Z, Xue H, Wang J, et al. Reduced Graphene Oxide/Marcasite - Type Cobalt Selenide Nanocrystals as an Anode for Lithium - Ion Batteries with Excellent Cyclic Performance. *ChemElectroChem*, 2015, 2(11): 1682-1686.
- [38] Li X, Zhang W, Feng Y, et al. Ultrafine CoSe nano-crystallites confined in leaf-like N-doped carbon for long-cyclic and fast sodium ion storage. *Electrochimica Acta*, 2019, 294: 173-182.
- [39] Yang J, Gao H, Men S, et al. CoSe₂ Nanoparticles Encapsulated by N - Doped Carbon Framework Intertwined with Carbon Nanotubes: High - Performance Dual - Role Anode Materials for Both Li - and Na - Ion Batteries. *Advanced Science*, 2018, 5(12): 1800763.
- [40] Mukkabl R, Deshagani S, Meduri P, et al. Selenium/graphite platelet nanofiber composite for durable Li-Se batteries. *ACS Energy Letters*, 2017, 2(6): 1288-1295.
- [41] Wei W, Yang S, Zhou H, et al. 3D graphene foams cross - linked with pre - encapsulated Fe₃O₄ nanospheres for enhanced lithium storage. *Advanced Materials*, 2013, 25(21): 2909-2914.

- [42] Zhou G, Wang D W, Li F, et al. Graphene-wrapped Fe_3O_4 anode material with improved reversible capacity and cyclic stability for lithium ion batteries. *Chemistry of Materials*, 2010, 22(18): 5306-5313.
- [43] Lou P, Cui Z, Jia Z, et al. Monodispersed carbon-coated cubic NiP_2 nanoparticles anchored on carbon nanotubes as ultra-long-life anodes for reversible lithium storage. *ACS Nano*, 2017, 11(4): 3705-3715.
- [44] Ge P, Zhang C, Hou H, et al. Anions induced evolution of Co_3X_4 (X= O, S, Se) as sodium-ion anodes: The influences of electronic structure, morphology, electrochemical property. *Nano Energy*, 2018, 48: 617-629.
- [45] Ma Y, Ma Y, Bresser D, et al. Cobalt disulfide nanoparticles embedded in porous carbonaceous micro-polyhedrons interlinked by carbon nanotubes for superior lithium and sodium storage. *ACS Nano*, 2018, 12(7): 7220-7231.
- [46] Zhang K, Park M, Zhou L, et al. Urchin - Like CoSe_2 as a high - performance anode material for sodium - ion batteries. *Advanced Functional Materials*, 2016, 26(37): 6728-6735.
- [47] Ali Z, Tang T, Huang X, et al. Cobalt selenide decorated carbon spheres for excellent cycling performance of sodium ion batteries. *Energy Storage Materials*, 2018, 13: 19-28.

Graphical abstract



CRedit author statement

Qingtao Wang: Writing- Reviewing and Editing, Project administration.

Minmin Hou: Methodology, Writing- Original draft preparation. **Dongxu Liu:** Writing - Review & Editing. **Xiaozhong Zhou:** Data curation. **Ziqiang Lei:** Supervision.

Journal Pre-proof

Declaration of interests

The authors declare that they have no known competing financial interests or personal relationships that could have appeared to influence the work reported in this paper.

The authors declare the following financial interests/personal relationships which may be considered as potential competing interests:

Journal Pre-proof

Highlights:

- The capacity of CoSe decreased first and then increased during charge/discharge.
- The reduction in capacity is related to the amorphousness of the CoSe material.
- The capacity increase is due to the recrystallization and the conductive SEI film.
- The rGO significantly reduced the capacity changes of CoSe during charge/discharge.
- The capacity of CoSe/rGO reaches 570 mA h g^{-1} after 1000 cycles under 1000 mA g^{-1} .